Title

A Combined Experimental and Numerical Modeling Study of the Deformation and Rupture of Axisymmetric Liquid Bridges under Coaxial Stretching.

Journal

Langmuir : the ACS journal of surfaces and colloids, 31(37)

ISSN

0743-7463

Authors

Zhuang, Jinda
Ju, Y Sungtaek

Publication Date

2015-09-01

DOI

10.1021/acs.langmuir.5b02102

Peer reviewed

A Combined Experimental and Numerical Modeling Study of the Deformation and Rupture of Axisymmetric Liquid Bridges under Coaxial Stretching

Jinda Zhuang, Y Sungtaek. Ju*

* Email: just@seas.ucla.edu

Mechanical and Aerospace Engineering Department, University of California, 420 Westwood Plaza, Los Angeles, CA 90095, U.S.A

Abstract: The deformation and rupture of axisymmetric liquid bridges being stretched between two fully wetted coaxial disks are studied experimentally and theoretically. We numerically solve the time-dependent Navier-Stokes equations while tracking the deformation of the liquid-air interface using the Arbitrary Lagrangian-Eulerian (ALE) moving mesh method to fully account for the effects of inertia and viscous forces on bridge dynamics. The effects of the stretching velocity, liquid properties, and liquid volume on the dynamics of liquid bridges are systematically investigated to provide direct experimental validation of our numerical model for stretching velocities as high as 3 m/s. The Ohnesorge number (*Oh*) of liquid bridges is a primary factor governing the dynamics of liquid bridge rupture, especially the dependence of the rupture distance on the stretching velocity. The rupture distance generally increases with the stretching velocity, far in excess of the static stability limit. For bridges with low Ohnesorge numbers, however, the rupture distance stay nearly constant or decreases with the stretching velocity within certain velocity windows due to the relative rupture position switching and the thread shape change. Our work provides an experimentally validated modeling approach and experimental data to help establish foundation for systematic further studies and applications of liquid bridges.

1. Introduction

The statics and dynamics of liquid bridges have been extensively studied for their importance in such diverse areas as crystal growth[1], spraying and atomization of liquids[2], fiber spinning[3], measurements of surface tension and viscosity[4], agglomeration of particles[5], and drop formation through capillary breakup[6]. Recent studies also investigated capillary forces mediated by liquid bridges for enhanced wet adhesion[7–12] and for self-alignment and self-assembly of milli- and sub-milliscale objects[13].

Many past studies of liquid bridges focused on their stability under near equilibrium or quasi-static conditions. Gillette et al.[14], for example, determined the limiting gap for the formation of a stable liquid bridge between two circular disks as a function of the liquid volume. A one-dimensional model was also developed by Rivas et al.[15] to characterize the evolution of liquid bridges around their stability limits.

Other studies examined the post-rupture behavior of liquid bridges, such as satellite droplet formation[16] and volume partitioning[17–19]. These phenomena are particularly relevant for printing industry. Chadov and Yakhnin[17,18], for example, investigated liquid bridge partitioning, illustrating preferential transfer of liquid to a more wettable surface. The amount of transferred liquid was also shown to increase with the difference in contact angle between the two surfaces. The separation speed and liquid properties, most notably viscosity and surface tension, also affected the volume partitioning.

The majority of these past studies of liquid bridges relied on quasi-static approximations to model their profiles, capillary forces, and rupture dynamics. This presents fundamental limitations, however, in modeling highly dynamic phenomena where the inertia and viscous effects cannot be ignored.

As an example, microscale liquid bridges have recently been explored as a potential enabler of reversibly switchable optical[20], mechanical, electrical and thermal interfaces[21–24] for micro and mesoscale devices. In these applications, liquid bridges can be subjected to repeated ruptures and reformations at rates in excess of 100 Hz. Fast rupture dynamics of liquid bridges also serves as a useful analogy for drop generation from a capillary tube. As another example, in capillary-mediated self-assembly processes, liquid bridge profiles were observed to continuously change and deviate noticeably from their equilibrium states.

This motivated studies of the dynamics of liquid bridges that accounted for the inertia and/or viscous effects. Early such studies, however, were limited as they used one-dimensional or inviscid flow approximations. Meseguer[1] studied axisymmetric liquid bridges that were

close to their stability limits using an inviscid slice model. The axisymmetric and non-axisymmetric oscillations of liquid bridges were theoretically investigated by Sanz et al[25,26]. Later studies investigated the effects of finite viscosity on the dynamics of liquid bridges under different conditions, including forced oscillations[27,28] and stretching[6,29]. The latter studies showed that even at modest elongation rates of 0.1 s^{-1}, instantaneous bridge shapes deviate considerably from equilibrium profiles and the limiting length can significantly exceed the critical length of a static bridge at its limit of stability.

Zhang et al.[6] used an one-dimensional (1D) model based on the slender jet assumption[30] to study the deformation and breakup of axisymmetric liquid bridges. The liquid bridges were held between two parallel coaxial disks of the same radius and subjected to stretching as the disks were continually pulled apart. The predicted interface profiles and rupture lengths agreed well with experimental data when stretching velocities were below U_c, which is the capillary velocity scale $(\sigma/\rho/R)^{1/2}$ (= 0.2 m/s for a water bridge of 1.6 mm radius). Here ρ and σ are the density and surface tension of the liquid, respectively and R is the radius of the disks. The capillary velocity scale measures the relative importance of inertial forces to surface tension forces.

A follow-up 2D modeling study[31] extended model predictions to higher stretching velocities and showed that the 1D model gave qualitatively and quantitatively different results from those of a presumably more accurate 2D model at stretching velocities > U_c. Direct experimental validation of the model predictions, however, was not reported.

Building upon these past studies, we report a combined experimental and numerical modeling study of the dynamics of axisymmetric liquid bridges that are coaxially stretched between two fully wetted disks. We focus on the deformation and rupture behavior of micro-scale liquid bridges over a much wider range of stretching velocities than the previous studies, up to 3 m/s. The dependence of the rupture length and rupture location on the stretching velocity, liquid properties, and liquid volume is systematically investigated. This work provides direct experimental validation of our numerical model based on a moving mesh method and offers physical insights useful for applying deformable microscale liquid elements as reversibly switchable mechanical or thermal interfaces.

2. Numerical Simulation

We consider the dynamics of an axisymmetric liquid bridge confined between two parallel fully-wetted circular disks of the identical radius R and surrounded by the ambient air. The top disk is moved upward along the common axis of symmetry at a velocity u whereas the bottom disk is stationary. The common axis of the symmetry of the bridge and the disks are aligned with the gravity vector. The radial coordinate of the air-liquid interface is denoted as h.

The transient liquid flows inside the bridge and the surrounding air are modeled using the Navier-Stokes equations and associated initial and boundary conditions. Figure 1 shows the simulation domains and boundary conditions used in our study. The liquid and the air are assumed to be incompressible with the constant density, viscosity and liquid-air interface surface tension.

We assume that the contact lines remain pinned at the disk edges:

$$h\,(z = 0,\, t) = R,\; h\,(z = L,\, t) = R \qquad (1)$$

and that the no slip condition holds at the disk surfaces:

$$u_r\,(z = 0\,,\, t) = 0,\; u_z\,(z = 0,\, t) = 0 \qquad (2)$$

$$u_r\,(z = L\,,\, t) = 0,\; u_z\,(z = L,\, t) = u \qquad (3)$$

For our experiments discussed later, we indeed observed no noticeable contact line motion, at least to within our optical resolution of approximately 20 μm. The pressure outlet condition is specified at the top, bottom and outer boundaries of the air domain.

The liquid bridge is assumed initially at rest in its equilibrium condition at volume v and initial length l_o.

$$h\,(z,\, t = 0) = h_{eq}\,(z) \qquad (4)$$

$$u_r\,(z,\, t = 0\,) = 0,\; u_z\,(z,\, t = 0\,) = 0 \qquad (5)$$

The Navier-Stokes equations are solved using a time-dependent finite-element solver based on the backward difference scheme. We employ the Arbitrary Lagrangian-Eulerian (ALE) moving mesh method[32,33] to handle dynamic deformation of the simulation domains and the moving boundaries. The evolution of the liquid-air interface is directly tracked using the instantaneous normal velocities of the fluid at the interface as obtained from solutions of the Navier-Stokes equations[34]. At each dynamically determined time step, new mesh coordinates are generated to account for the movement of the boundaries.

The mesh quality gradually degrades as the simulation domains deform. An automatic remeshing method is adopted to periodically generate a new mesh when the mesh quality index falls below a threshold value. The maximum allowed time step is limited to $10^{-6}/u$ where u is the stretching velocity. The liquid volume is monitored during the entire simulation process to confirm that any variation stays below 0.1%.

A typical simulation run starts with a liquid bridge at its equilibrium state as obtained by setting the stretching velocity u to zero. A predefined temporal velocity profile is next applied to the top disk to emulate a stretching process. The bridge shapes (as defined by the locations of the air-liquid interface) and the velocity and pressure distributions are recorded at each time step until rupture occurs. The liquid bridge is considered ruptured when

the minimum radius of the liquid bridge at any point along its length reaches 0.01% of the disk radius R.

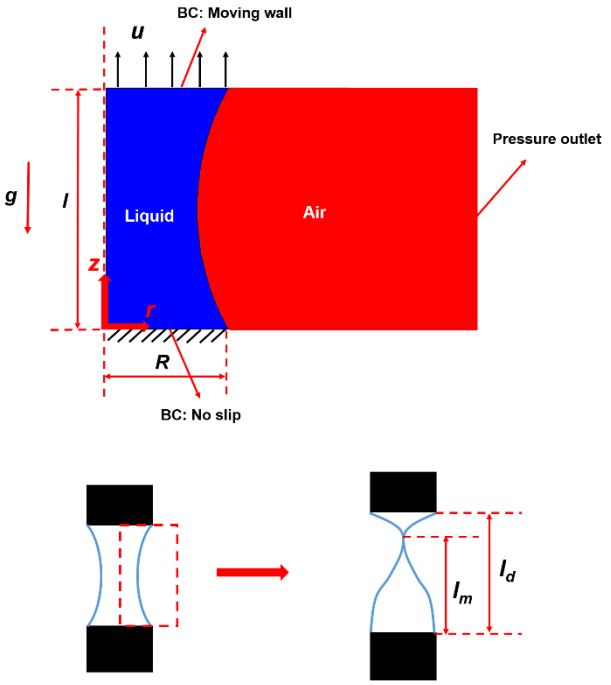

Figure 1. Schematic of the simulation domains and boundary conditions used to model an axisymmetric liquid bridge, which is held between two parallel coaxial disks of equal radii R (not shown) and stretched at a velocity of u. We define a cylindrical coordinate system {r, z} whose origin is located at the center of the bottom disk. The rupture distance and the rupture location are noted as l_d and l_m, respectively.

Test simulation runs were conducted with a very small disk velocity (0.001 mm/s) to confirm that we can replicate static stability limits predicted by the surface energy minimization algorithm[7] (see Supporting Information). We further confirmed that the rupture distances predicted by our numerical simulation agree with the values reported for moderate stretching velocities by Yildirim and Basaran[31] to within 2%.

A mesh independence study was also carried out. We confirmed that doubling the number of mesh elements results in less than 1% changes in the predicted rupture distances and partial liquid volumes.

To help generalize our results, we normalize relevant variables using the disk radius R as the characteristic length scale of the system and $U_c = (\sigma/\rho/R)^{1/2}$ as the characteristic velocity scale. The corresponding characteristic time scale is $t_c = (\rho R^3/\sigma)^{1/2}$. The governing dimensionless groups are: 1) the dimensionless stretching velocity $U \equiv \sqrt{\rho R u^2/\sigma}$; 2) the Ohnesorge number $Oh \equiv \mu/\sqrt{\rho R \sigma}$; 3) the Bond number $Bo \equiv g\rho R^2/\sigma$; 4) the dimensionless initial bridge length $L_0 \equiv l_0/R$; 5) the dimensionless liquid volume $V \equiv v/\pi R^3$.

The dimensionless stretching velocity can be re-expressed as $U = \sqrt{We}$, where We is the Weber number. The Weber number measures the importance of inertial force over surface tension force. The Ohnesorge number Oh measures the importance of viscous force over surface tension force and the Bond number Bo measures the importance of gravitational force over surface tension force. Since we are most interested in the dynamics of sub-millimeter and microscale liquid bridges, the Bond number is kept small ($Bo < 0.05$). We note that the Bond number may alternatively be defined as $Bo \equiv g\rho l^2/\sigma$, where l is the length of the liquid bridge. This may reflect the effect of the gravity more accurately but it is not convenient to use as the bridge length changes with time. The particular definition of the Bond number used should not affect our results as the gravity is explicitly accounted for in our numerical simulation.

3. Experiments

Experiments are conducted to allow direct validation of our predictions from the 2D axisymmetric model. To achieve stretching velocities as high as 3 m/s, we have developed an impact-driven setup schematically illustrated in Fig. 2. The liquid bridge is held between the parallel surfaces of two cylindrical stainless steel disks of the same radius. The disks are coaxial with the liquid bridge. The disk radius R is fixed at 0.5 mm for all the results reported in the article. The parallel surfaces of the disks are machined flat and held perpendicular to the disk axis so that the liquid completely wets the surfaces and the contact lines remain pinned on the sharp edges of the disk surfaces.

The bottom disk is fixed and the top disk is attached to a plate that can move vertically along a cylindrical slide guide. A high-striker mechanism is implemented to apply impact to this movable plate. A weight released from a certain height accelerates as it falls and activates a striker, which is coaxial with a movable plate. The plate and hence the upper disk then accelerate to a target velocity, typically within 1 ms. By changing the initial height of the falling weight, different stretching velocities can be achieved.

In a typical experimental run, two disks are first separated by a target initial distance. A liquid bridge is next formed by depositing a desired amount of liquid into the space between the two disks using a pipette with a resolution of 0.002 μL. The liquid bridge is next allowed to relax into its equilibrium state. We independently confirm the liquid volume by integrating the bridge cross section obtained through optical imaging under the assumption that the liquid bridge is axisymmetric. In one reproducibility study, the maximum difference between the targeted and measured liquid volumes were 3% over 10 independent measurements. The measured rupture distances varied by less than 5 % over these measurements.

A high speed camera (FASTCAM MC2, Photron Inc.) with a frame rate of 8000 fps is used to capture temporal trajectories of the upper disk and variations in the bridge shape. The acquired digital images are analyzed using Matlab and ImageJ to extract the instantaneous positions

of the upper disk and the liquid-air interface. Representative temporal velocity profiles of the upper disk are shown in Fig. 3.

For each experimental condition, measurements were repeated at least 4 times to ascertain the reproducibility of the results.

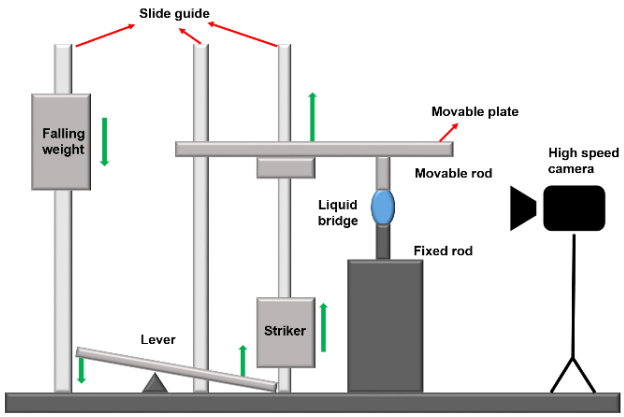

Figure 2. Schematic of the experimental setup used to uniaxially stretch the liquid bridge at varying stretching velocities.

To investigate the effects of the physical properties of the liquid, aqueous solutions of glycerol at different weight concentrations (0%, 20%, 40%, 60%, 80%) are used[35]. The densities and surface tensions of the aqueous solutions are similar to each other, varying by less than 30%, whereas their viscosities vary by more than three orders of magnitude. This allows us to explore large variations in the *Oh* number while maintaining the Bond number relatively constant.

Experiments were performed for different values of the velocity of the upper disk, liquid properties, and initial liquid bridge lengths. The Ohnesorge number ranges from 0.002 to 0.5, the disk velocity from 0.1 m/s to 3 m/s, and the initial dimensionless bridge length L_o from 0.2 to 3. The dimensionless liquid volume V is fixed at 2.

While one can readily assign arbitrary temporal velocity profiles in numerical simulations, achieving infinite acceleration and maintaining a constant disk velocity in real experiments is not feasible due to finite inertia, gravity and friction.

To help present and interpret our data, we therefore performed two sets of simulations using two different sets of velocity profiles. The first set of velocity profiles (actual profiles) is obtained by analyzing the trajectories of the upper disk for direct comparison with the experimentally determined bridge profiles and rupture distances. The second set of velocity profiles is approximate idealized velocity profiles (idealized profiles) that consist of the linear ramp up phase and the constant "average" velocity phase. Simulations based on these idealized profiles are meant to help identify general trends. The average velocity is set to match the total distance traveled by the upper disk up to a bridge rupture point. Figure 3 shows representative actual and corresponding ideal velocity profiles, which are input into our numerical simulations.

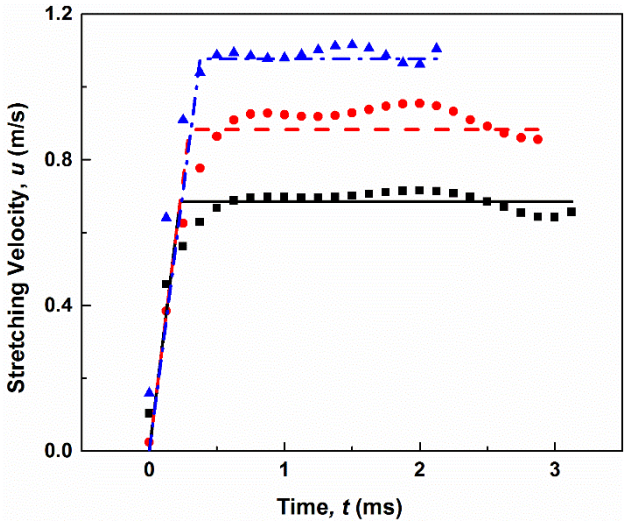

Figure 3. Representative actual (symbols) and idealized (lines) temporal velocity profiles of the upper disk.

4. Results and discussion

The dynamics of a stretching liquid bridge of a given dimensionless initial length L_o is governed by the dimensionless groups defined earlier: the Ohnesorge number *Oh*, the dimensionless stretching velocity U (or the Weber number $We = U^2$), the Bond number *Bo*, and the dimensionless bridge volume V.

4.1 Dynamic deformation of liquid bridges

We first compare the predicted liquid bridge profiles with the experimentally measured profiles for liquid bridges with a low (0.05) and a high (0.5) Ohnesorge number. The dimensionless stretching velocity U is fixed at 1 ($U = 1$). All the results presented in the article have been obtained for liquid bridges with $L_o = 2$ (see Supporting Information for the impact of *Lo* on the dependence of the rupture distance on the stretching velocity).

Figure 4 shows the temporal evolution of the simulated and experimentally measured shapes and minimum neck radius of the liquid bridge with an Ohnesorge number of 0.05 (a 60% glycerol solution). As shown in the inset, the instant the bridge is stretched, necking first occurs in the upper portion of the liquid bridge. As the stretching continues, the necked portion of the liquid bridge gradually contracts further, ultimately leading to rupture. As the liquid bridge breaks up, the upper portion of the bridge forms a near spherical droplet whereas the lower portion of the bridge develops an elongated liquid thread. The temporal evolution of the dimensionless minimum neck radius h_{min}/R is shown in Fig. 4. The neck radius decreases at higher rates in the early stage of stretching than near rupture partly because further increase in the capillary pressure is opposed by the inertia and viscous effects.

Figure 5 shows the corresponding results for a liquid bridge with a higher Ohnesorge number (0.5 for an 80% Glycerol solution). The liquid bridge again first contracts at its upper portion but then develops into an almost symmetric (top to bottom) vase-like shape. A long cylinder-like liquid thread develops for the bridge with the higher Ohnesorge number. The liquid thread only gradually thin down as the stretching continues. As a result, the rupture time is significantly longer than that for the bridge with the smaller Ohnesorge number. The different manners in which the two liquid bridges evolve suggest one way to control the rupture of liquid bridges by simply choosing liquids with different Ohnesorge numbers.

For both cases, the experimental results and numerical predictions agree reasonably well in terms of the bridge shape and also the minimum neck radius. The maximum deviation is approximately 3%.

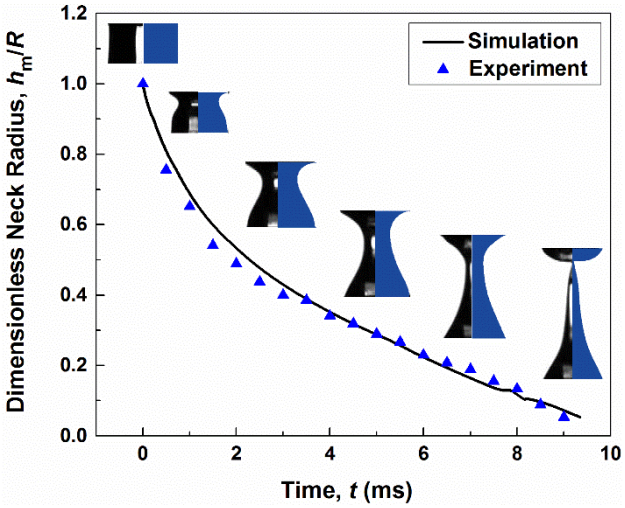

Figure 4. Temporal evolution of the predicted and experimentally determined minimum neck radius and bridge profiles (inset images) for a bridge with an Ohnesorge number of 0.05 (a 60% glycerol solution).

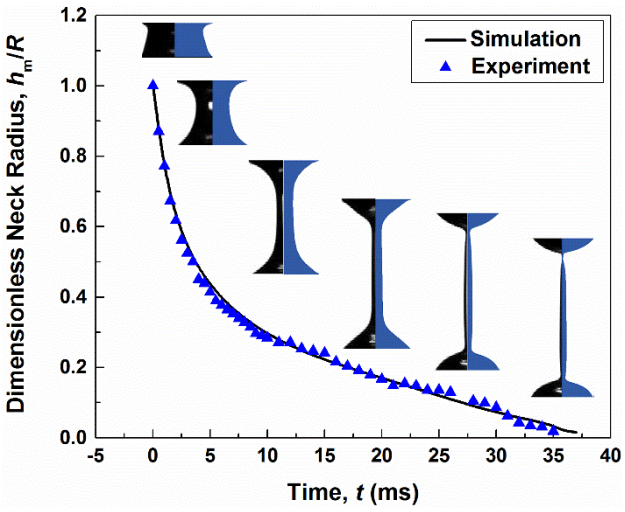

Figure 5. Temporal evolution of the predicted and experimentally determined minimum neck radius and bridge profiles (inset images) for a bridge with an Ohnesorge number of 0.5 (an 80% glycerol solution).

We note that, although the temporal evolution of the minimum neck radius is qualitatively similar for the two cases with different Ohnesorge numbers, the underlying details of the dynamics are very different. To gain further insights into the dynamics of liquid bridge rupture, we next examine internal pressure distributions.

Figure 6 shows the numerically computed liquid bridge profiles and corresponding internal pressure distributions for low and high Ohnesorge number cases. The dimensionless pressure within a liquid bridge is given, to the leading order, by $2H/Oh - \partial U_z/\partial z$. Here, H is the local mean curvature of the interface and U_z is dimensionless velocity in the z direction[31]. The capillary pressure $2H/Oh$ and the viscous pressure $\partial v_0/\partial z$ compete to determine the total pressure within the liquid bridge.

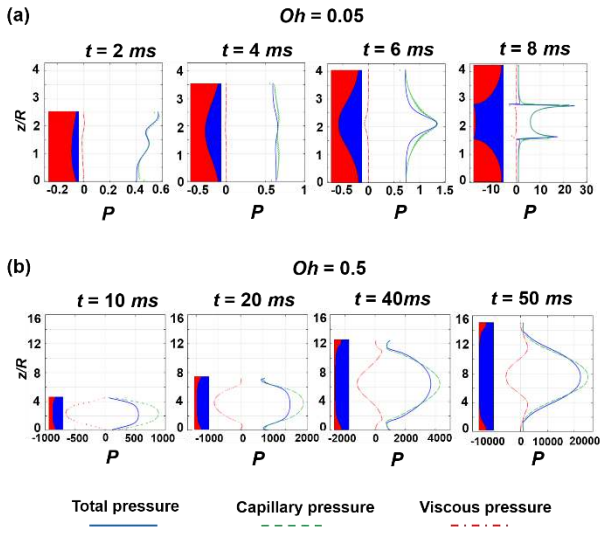

Figure 6. The predicted dimensionless pressures and liquid bridge profiles for a) Ohnesorge number Oh = 0.05 and b) Ohnesorge number Oh = 0.5. The dimensionless stretching velocity U is fixed at 1.

For the liquid bridge with the lower Ohnesorge number (Fig. 6a), the viscous pressure is negligible compared with the capillary pressure. As a result, the bridge generally follows a curvature-controlled rupture process. The bridge develops a necking point and the liquid is rapidly expelled away from this point due to high spatial capillary pressure gradients. This leads to a rapid bridge break up and a small rupture length.

For the liquid bridge with the higher Ohnesorge number (Fig. 6b), the viscous pressure can be comparable to the capillary pressure. It effectively opposes the capillary pressure gradient that expels the liquid away from the center. This drastically changes the total pressure profile. The pressure within the bridge is more uniformly distributed and virtually symmetric. No pronounced necking point with a distinct large curvature is developed. Instead, the liquid bridge supports a long

stable liquid thread, which gradually thins down until the bridge ruptures. This stabilizing effect of the viscous force delays rupture and leads to larger rupture distances.

4.2 Rupture distance: the effects of *U* and *Oh*

We next examine the effects of the Ohnesorge number *Oh* and the dimensionless stretching velocity *U* (or Weber number) on the rupture dynamics of liquid bridges.

We first discuss simulation results where the Bond number is set to be zero to remove any complication from the gravitational effect. This is reasonable for micro-scale liquid bridges. Numerical simulations are performed over a wide range of stretching velocities for liquid bridges with different Ohnesorge numbers. As a reminder, the rupture distance is nondimensionalized as $L_d = l_d/R$, where l_d is the separation of the two disks at the point of bridge rupture. The dimensionless rupture location is defined as $L_m = l_m/R$, where l_m is the vertical distance from the rupture point to the bottom disk (Fig. 1).

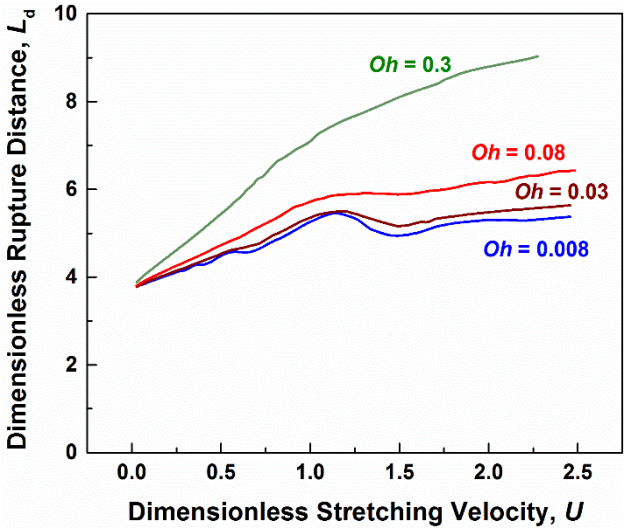

Figure 7. Predicted rupture distance L_d as a function of the stretching velocity *U* for liquid bridges with different values of the Ohnesorge number. The Bond number *Bo* is set to be zero.

The predicted dimensionless rupture distance L_d is shown in Fig. 7 as a function of the stretching velocity *U* for different values of the Ohnesorge number. When a liquid bridge is axially stretched at a very low velocity, the bridge shape at each instant closely resembles the quasi-equilibrium shape that it would have if the moving disk were instantaneously brought to rest and the bridge were allowed to relax to its equilibrium state. Under this condition, the rupture distance that the bridge attains exceeds the maximum stable length of a nominally identical static bridge by only a small amount. The rupture distance is also relatively insensitive to the Ohnesorge number. This is consistent with well-established static stability of liquid bridges[36] and prior experimental measurements at low stretching velocity (< 6 mm/s)[6]. In contrast, at higher stretching velocities, the departure of the transient shapes from the equilibrium ones becomes larger and the rupture distance is increased substantially over the maximum stable length of a comparable static bridge.

For a liquid bridge with a relatively small value of *Oh* (0.008), rather complex trends are observed in the dependence of it rupture distance on the stretching velocity. These are represented by the *relative* rupture location switching and the liquid thread shape changes. Figure 8 shows a zoomed view of the rupture distance plot with matching bridge profiles illustrating these two phenomena.

As mentioned before, at very small stretching velocities, a liquid bridge approximately maintains its quasi-static state. Rupture occurs almost simultaneously at the upper and lower necking points. As the stretching velocity increases, however, the rupture location shifts.

For liquid bridges with small values of *Oh*, the rupture process is governed primarily by localized peaks in the capillary pressure. The rupture occurs at or near the maximum local mean curvature point(s). Two potential rupture points (one closer to the top disk; the other closer to the bottom disk) exist due to the opposite signs of the two principle curvature components contributing to the total local mean curvature. We will refer to them as the upper and lower potential rupture point, respectively.

As the stretching velocity is increased, rupture occurs first on the lower potential rupture point (Fig. 8 inset I). As the stretching velocity is further increased, the rupture location switches to the upper point (Fig. 8 inset III). We call this the relative rupture point switching. There may be additional rupture location switching events (back to the lower point and then to the upper point) as the stretching velocity is further increased for bridges with relatively low Ohnesorge numbers. The rupture distance stays relatively constant or drops slightly with increasing stretching velocity during these switchings.

One consequence of the rupture location switching is on the trajectory of satellite droplets formed after a liquid bridge ruptures. These satellite droplets may either recoil toward the residual droplet on the bottom disk or the top disk depending in part on the relative rupture location[31].

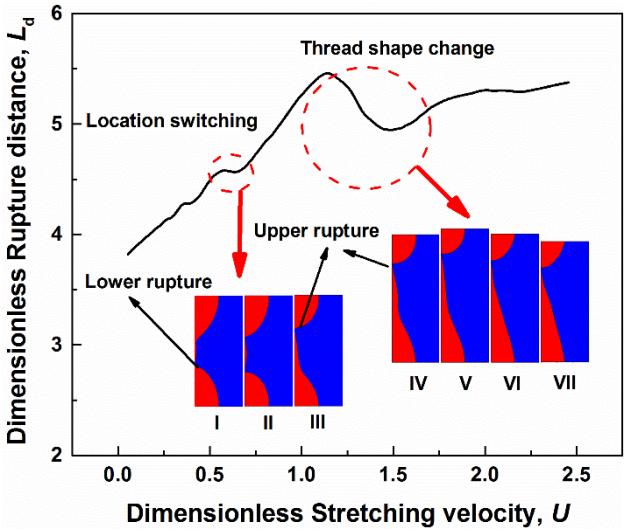

Figure 8. The predicted rupture distance as a function of the dimensionless stretching velocity (The case of Oh = 0.008 in Fig. 7). The insets illustrate the rupture location switchings and the thread shape change discussed in the text.

When the stretching velocity becomes large enough and the inertia effect is significant, a pronounced necking develops near the upper portion of the liquid bridge almost immediately after the upper disk is set into motion. This leads to a thin necked portion with a large local mean curvature. The liquid bridge then always ruptures at this upper portion (Fig. 8 insets IV-VII).

We consider the transition velocity U_{tr}, approximately 1 in Fig. 8, as the velocity above which no further rupture location switching happens for bridges with a given value of Oh. That is, the liquid bridges always rupture at the upper rupture points at velocities larger than this transition velocity. Additional simulation (see Figure S5 in Supporting Information) suggests that this transition velocity is weakly dependent on the Ohnesorge number but is a function of the aspect ratio of the initial liquid bridge (i.e., the dimensionless bridge length, $L_o/2 = l_o/2R$).

At still higher stretching velocities, even though the rupture points stay in the upper portion of the liquid bridge, we observe an additional anomaly in the stretching velocity dependence. That is, the liquid thread in the lower portion of the liquid bridge exhibits a change in shape from a long and thin needle-like structure (Fig. 8 insets IV-V) to a short and thick cone-like structure (Fig. 8 insets VI-VII). Accompanying this shape change is reduction in the rupture distance with increasing stretching velocity. In the long needle-like structure, locally enhanced capillary pressure gradients around the lower potential rupture point cause the liquid to be expelled, leading to the formation of an elongated liquid thread of varying widths. In the short and thick cone-like structure, in contrast, the lower potential rupture point becomes insignificant and the thread stays short.

Aside from these localized anomalies, the rupture distance generally increases with stretching velocity. This overall trend is consistent with the stabilizing effect of increasing inertial force over surface tension force as measured by the dimensionless velocity U (or Weber number $We = U^2$).

For liquid bridges with the larger Ohnesorge numbers (Oh = 0.08 and 0.3 in Fig. 7), localized anomalies are less obvious, all but indiscernible for the highest Oh considered. Increasing Oh (for example, by increasing the viscosity and/or reducing the surface tension) has added stabilizing effects on the liquid bridge, enabling the formation of highly elongated liquid threads.

We next compare our experimental results with the numerical model predictions for liquid bridges of different values of Oh. Figure 9 shows the experimentally captured and predicted liquid bridge profiles right before rupture for different stretching velocities. Liquid bridges with Oh = 0.005, 0.05 and 0.5 are considered. For a low Oh (A: Oh = 0.005) liquid bridge, the rupture position switching (I to III) and the thread shape change (IV to VI) are observed as predicted in our simulations. These phenomena are less obvious as the Oh number increases (B: Oh = 0.05) and all but disappear when Oh is sufficiently high (C: Oh =0.5). The transition from the rupture location switching regime to the thread shape change regime occurs between Columns II and III in Fig. 9 or for stretching velocities of approximately 1 for the cases considered in the present study (see Fig. S5 in Supporting Information for further discussion). The experimental results agree reasonably well with the predictions.

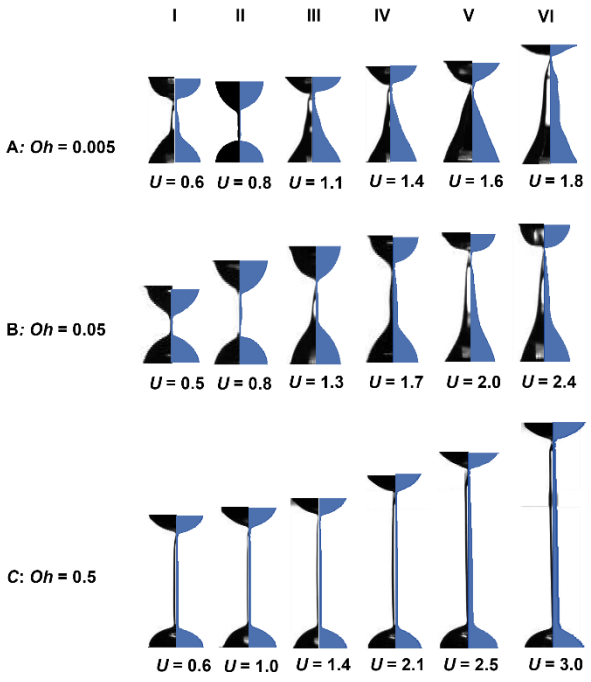

Figure 9. Comparison between the experimentally captured and predicted liquid bridge profiles right before rupture for different stretching velocities. Results are from liquid bridges with Oh = 0.005, 0.05, and 0.5.

Figure 10 compares the experimentally measured and predicted dimensionless rupture distances as a function

of the dimensionless stretching velocity for liquid bridges with a low value of *Oh* (= 0.005). The experiments are repeated four independent times and we report the average values as the filled triangles in Fig. 10. Standard deviations are reported as error bars.

The hollow symbols in Fig. 10 correspond to the simulation results obtained using actual velocity profiles obtained for each individual experimental condition. The corresponding individual experimental results are shown as the filled diamonds. They agree reasonably well with < 10% deviation.

To help clarify a general trend, we also show the simulation results obtained using "idealized" temporal velocity profiles (Section 3, Fig. 3) as the solid line.

Figure 11 shows similar comparison for liquid bridges of a moderate value of *Oh* (= 0.05). The increase in *Oh* is mainly due to a larger viscosity of the liquid used (a 60% glycerol solution). One can notice almost monotonic increase in the rupture distance with the increasing stretching velocity. Local anomalies (the rupture location switching and the thread shape change) are barely distinguishable. Again, reasonable agreement is observed between the predicted and experimental results.

For the liquid bridge with the highest value of *Oh* we considered (Fig. 12), the rupture distance increases monotonically with the stretching velocity throughout the entire velocity range considered. Compared with the other liquid bridges with the lower Ohnesorge numbers, a drastically longer liquid thread is developed. As a result, the rupture distance is significantly larger for a given stretching velocity.

The observation that liquid bridges with different Ohnesorge numbers show distinct rupture behaviors can be taken advantage in designing practical devices. For example, one may choose high *Oh* liquid bridges to achieve highly stretchable liquid interconnections for flexible or reconfigurable electronic and optoelectronic devices. Alternatively, one may wish to minimize the rupture distance for fast switching of thermal or electrical conductance by identifying a local minimum in the rupture distance around the thread shape change regime.

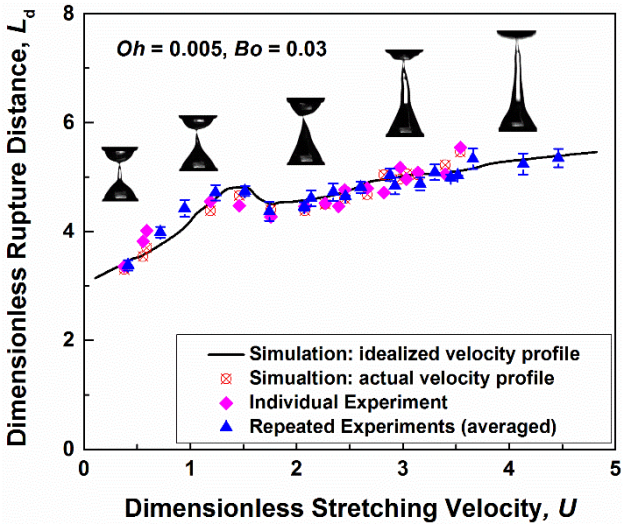

Figure 10. Predicted and experimentally determined dimensionless rupture distance as a function of the dimensionless stretching velocity. The bridge is made of water (*Oh* = 0.005, *Bo* = 0.03). Superposed on the plot are experimentally obtained images of the liquid bridge at the incipience of rupture at several different stretching velocities.

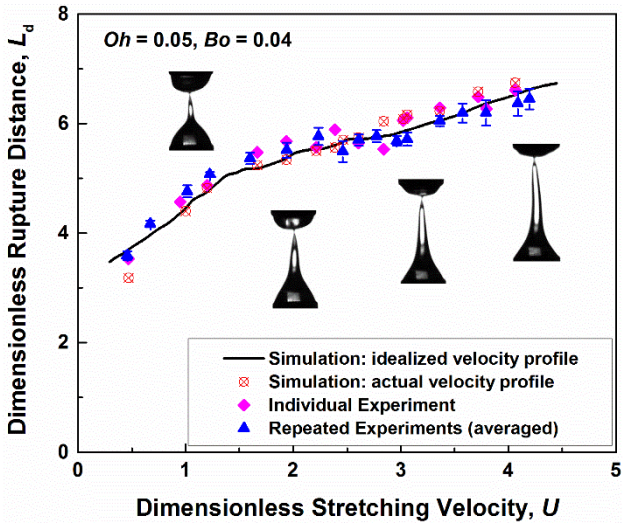

Figure 11. Predicted and experimentally determined dimensionless rupture distance as a function of the dimensionless stretching velocity. The bridge is made of a 60% glycerol solution (*Oh* = 0.05, *Bo* = 0.04). Superposed on the plot are experimentally obtained images of the liquid bridge at the incipience of rupture at select stretching velocities.

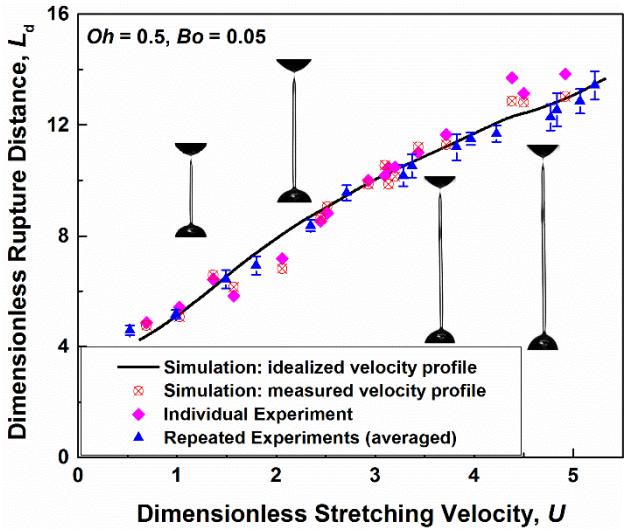

Figure 12. Predicted and experimentally determined dimensionless rupture distance as a function of the dimensionless stretching velocity. The bridge is made of an 80% glycerol solution (*Oh* = 0.5, *Bo* = 0.05). Superposed on the plot are experimentally obtained images of the liquid bridge at the incipience of rupture at select stretching velocities.

We note that all the results presented in the article are obtained under asymmetric stretching conditions where only the top disk is in motion and the bottom disk remains stationary. Under the symmetric stretching condition, the top and bottom disks would be stretched in opposing directions, each at half the total target stretching speed. At higher stretching velocities, where the inertia effects are significant, the rupture distances under the symmetric and asymmetric stretching conditions significantly deviate from each other (see Supporting Information). The symmetric stretching condition suppresses the development of pronounced upper potential rupture points and associated local anomalies.

The experimentally measured and predicted rupture distances as a function of *Oh* for different stretching velocities are shown in Fig. 13. Similar results have been reported in previous experimental[6] and numerical modeling[31] studies but only at relatively low stretching velocities. Setting aside experimental uncertainties, for a given stretching velocity, we note that the rupture distance is rather insensitive to *Oh* when $Oh < 0.01$. Relatively speaking, it increases more rapidly with *Oh* when $Oh > 0.01$ as the rupture behavior changes from the capillary controlled necking to the viscous controlled thread thinning. The experimental results agree reasonably well with the predictions with deviation < 5 %.

We note in passing that we did not observe any "premature" rupture of liquid bridges that resulted in smaller rupture distances than what we predicted. This may, however, be due to a specific set of experimental approaches/protocols we used. Under certain other conditions (for example, plates and/or liquid bridges are subjected to mechanical, electrical, or magnetic oscillations in addition to unidirectional stretching at a constant speed) one may potentially observe accelerated bridge rupture.

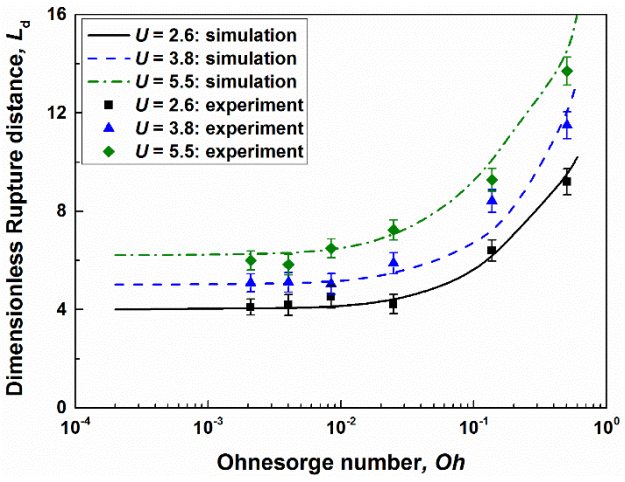

Figure 13. Predicted (lines) and experimental (symbols) results of the dimensionless rupture distance as a function of the Ohnesorge number for different stretching velocities.

4.3 Relative Rupture Location and Partial Liquid Volume

In Section 4.2, we discussed the relative rupture location switching as local anomalies observed in the stretching velocity dependence of the rupture distance. To illustrate this more systematically, we show the predicted and experimentally measured relative rupture locations L_m/L_d in Fig. 14 as a function of the dimensionless stretching velocity. Results are shown for bridges made of water and an 80% glycerol solution. We refer to cases where $L_m/L_d > 0.5$ as the upper point rupture mode and cases where $L_m/L_d < 0.5$ as the lower point rupture mode. For liquid bridges with a low value of *Oh* (e.g. water), the rupture location switches between the upper and lower potential rupture points at relatively low stretching velocities. When the stretching velocity is sufficiently large ($U > 1$), the rupture location switches back to and remains on the upper portion of the bridge. A similar trend is observed for a liquid bridge with a higher value of *Oh* (80% glycerol solution) but with much smaller variations in the relative rupture distance as the switchings occur.

Another parameter of interest is the partial residual volume V_p, which is defined as the ratio of the volume V_b of the liquid remaining on the bottom disk after rupture and the total liquid volume V. Figure 15 shows variation in the partial volume as a function of the dimensionless stretching velocity for liquid bridges with different values of *Oh*. Under static conditions or extremely small stretching velocities, the partial volume is approximately 0.5 as the bridge breaks up symmetrically. Note that the two disks are nominally identical with the same contact angles in all cases considered in the present study. The symmetric rupture is consistent with the results of previously reported liquid partitioning studies[17–19].

As the stretching velocity increases, the relative rupture location switches between the lower to the upper potential rupture points. For the lower point rupture cases, the partial volume is less than 0.5 and the larger portion of the liquid will remain pendant to the top disk. For the upper point rupture cases, the partial volume is larger than 0.5 at higher stretching velocities as a larger portion of the liquid forms a long thread at the bottom.

Note that the rupture distance anomaly caused by the thread shape change does not influence the increase in the partial volume with increasing stretching velocity. As inertial effects become dominant over surface tension effects, more liquid remains on the lower portion of the liquid thread despite such a shape change.

For the liquid bridge with the higher *Oh* (an 80% glycerol solution), the partial volume remains relatively insensitive to the stretching velocity when the velocity is relatively small. As the relative rupture location switches from the lower to the upper potential rupture points, the partial volume increases with the stretching velocity. Compared with the bridge with the lower *Oh*, the effects of the rupture location switching and thread shape change on the partial volume is less pronounced due to the damping effect of viscosity over surface tension.

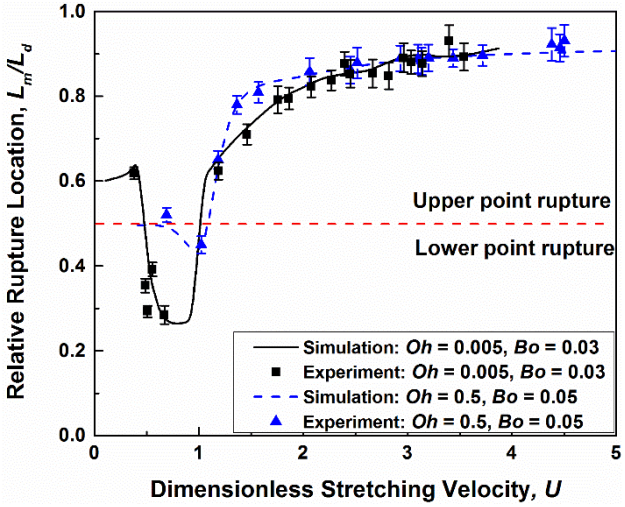

Figure 14. Simulation and experimental results of the partial volume as a function of the stretching velocity for water (Oh = 0.005, Bo = 0.03) and an 80% Glycerol solution (Oh = 0.5, Bo = 0.05).

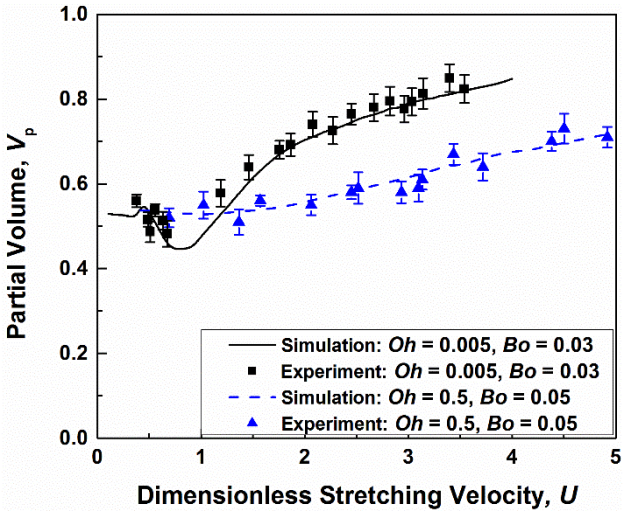

Figure 15. Simulation and experimental results of the partial volume as a function of the stretching velocity for water (Oh = 0.005, Bo = 0.03) and an 80% Glycerol solution (Oh = 0.5, Bo = 0.05).

5. Summary and Conclusion

In this paper, the effects of inertial, viscous and surface tension forces on the dynamics of stretching liquid bridges are investigated using a combined experimental and numerical simulation study. The experiments and simulations are carried out for a wide range of dimensionless stretching velocities and Ohnesorge numbers. The rupture distance of a liquid bridge generally increases with stretching velocity due in part to the stabilizing effect of viscous and inertia force. For low-Oh liquid bridges, local anomalies in the rupture distance, such as the relative rupture position switching and the thread shape change, occur as the stretching velocity is varied. Such anomalies are less visible for high-Oh liquid bridges. The partial volume of the liquid remaining on the bottom disk after rupture generally increases with increasing stretching velocity. Our study provides direct experimental validation of the numerical simulation approach based on the moving mesh scheme for capturing dynamics of capillary confined liquid bridges and their rupture. Our work helps develop a systematic design tool for utilizing liquid bridges as mechanical, electrical or thermal interfaces.

The present study focused exclusively on axisymmetric liquid bridges formed between two identical full-wetted disks. We note, however, that contact line motions on more general solid substrates can significantly affect the statics and dynamics of liquid bridge[37], including the bridge deformation and rupture patterns[19,38]. Further studies on this rich topic, including accurate modeling of the mechanics of contact line pinning and unpinning[39] would be worthy extension of our work.

References

(1) Meseguer, J. The Breaking of Axisymmetric Slender Liquid Bridges. *J Fluid Mech 130*, 123.

(2) Schulkes, R. M. S. M. Nonlinear Dynamics of Liquid Columns: A Comparative Study. *Phys. Fluids Fluid Dyn. 1989-1993* **1993**, *5* (9), 2121–2130.

(3) Tirtaatmadja, V.; Sridhar, T. A Filament Stretching Device for Measurement of Extensional Viscosity. *J. Rheol. 1978-Present* **1993**, *37* (6), 1081–1102.

(4) Spiegelberg, S. H.; Ables, D. C.; McKinley, G. H. The Role of End-Effects on Measurements of Extensional Viscosity in Filament Stretching Rheometers. *J. Non-Newton. Fluid Mech.* **1996**, *64* (2–3), 229–267.

(5) Chen, T.-Y.; Tsamopoulos, J. A.; Good, R. J. Capillary Bridges between Parallel and Non-Parallel Surfaces and Their Stability. *J. Colloid Interface Sci.* **1992**, *151* (1), 49–69.

(6) Zhang, X.; Padgett, R. S.; Basaran, O. A. Nonlinear Deformation and Breakup of Stretching Liquid Bridges. *J. Fluid Mech.* **1996**, *329*, 207–245.

(7) De Souza, E. J.; Brinkmann, M.; Mohrdieck, C.; Crosby, A.; Arzt, E. Capillary Forces between Chemically Different Substrates. *Langmuir* **2008**, *24* (18), 10161–10168.

(8) Broesch, D. J.; Dutka, F.; Frechette, J. Curvature of Capillary Bridges as a Competition between Wetting and Confinement. *Langmuir* **2013**, *29* (50), 15558–15564.

(9) De Souza, E. J.; Brinkmann, M.; Mohrdieck, C.; Arzt, E. Enhancement of Capillary Forces by Multiple Liquid Bridges. *Langmuir* **2008**, *24* (16), 8813–8820.

(10) Kusumaatmaja, H.; Lipowsky, R. Equilibrium Morphologies and Effective Spring Constants of Capillary Bridges. *Langmuir* **2010**, *26* (24), 18734–18741.

(11) Broesch, D. J.; Frechette, J. From Concave to Convex: Capillary Bridges in Slit Pore Geometry. *Langmuir* **2012**, *28* (44), 15548–15554.

(12) Virozub, A.; Haimovich, N.; Brandon, S. Three-Dimensional Simulations of Liquid Bridges between Two Cylinders: Forces, Energies, and Torques. *Langmuir* **2009**, *25* (22), 12837–12842.

(13) Arutinov, G.; Smits, E. C. P.; Albert, P.; Lambert, P.; Mastrangeli, M. In-Plane Mode Dynamics of Capillary Self-Alignment. *Langmuir* **2014**, *30* (43), 13092–13102.

(14) Gillette, R. D.; Dyson, D. C. Stability of Fluid Interfaces of Revolution between Equal Solid Circular Plates. *Chem. Eng. J.* **1971**, *2* (1), 44–54.

(15) Meseguer Ruiz, J.; Rivas, D. One-Dimensional Self-Similar Solution of the Dynamics of Axisymmetric Slender Liquid Bridges. *J. Fluid Mech.* **1984**, *138*, 417–429.

(16) M. Tjahjadi, H. A. S. Satellite and Subsatellite Formation in Capillary Breakup. *J. Fluid Mech.* **1992**, *243*, 297–317.
(17) Chadov, A. V., Yakhnin, E. D. Study of Liquid Transfer from One Hard Surface to Another. I. Equilibrium Transfer. Method of Approximate Calculation. *Colloid J Russ. Acad. Sci.* **1979**, *47*, 817.
(18) Yakhnin, E. D., Chadov, A. V. Study of the Transfer of Liquid from One Solid Surface to Another. 2. Dynamic Transfer. *Colloid J Russ Acad Sci* **1983**, *45*, 1183.
(19) Kumar, S. Liquid Transfer in Printing Processes: Liquid Bridges with Moving Contact Lines. *Annu. Rev. Fluid Mech.* **2015**, *47* (1), 67–94.
(20) Hu, B.; Xue, L.; Yang, P.; Han, Y. Variable-Focus Liquid Microlenses with Adjustable 3-D Curved Housings. *Langmuir* **2010**, *26* (9), 6350–6356.
(21) Jia, Y.; Cha, G.; Ju, Y. S. Switchable Thermal Interfaces Based on Discrete Liquid Droplets. *Micromachines* **2012**, *3* (1), 10–20.
(22) Cha, G.; Ju, Y. S. Reversible Thermal Interfaces Based on Microscale Dielectric Liquid Layers. *Appl. Phys. Lett.* **2009**, *94* (21), 211904.
(23) Timonen, J. V. I.; Latikka, M.; Leibler, L.; Ras, R. H. A.; Ikkala, O. Switchable Static and Dynamic Self-Assembly of Magnetic Droplets on Superhydrophobic Surfaces. *Science* **2013**, *341* (6143), 253–257.
(24) Zhan, Y.; Cha, G.; Zhuang, J.; Jia, Y.; Ju, Y. S. Microscale Liquid-Based Mechanical Elements for Multifunctional Integration. *J. Compos. Mater.* **2013**, *47* (1), 65–75.
(25) Sanz, A.; Diez, J. L. Non-Axisymmetric Oscillations of Liquid Bridges. *J. Fluid Mech.* **1989**, *205*, 503–521.
(26) Sanz, A. The Influence of the Outer Bath in the Dynamics of Axisymmetric Liquid Bridges. *J. Fluid Mech.* **1985**, *156*, 101–140.
(27) Tsamopoulos, J.; Chen, T.-Y.; Borkar, A. Viscous Oscillations of Capillary Bridges. *J. Fluid Mech.* **1992**, *235*, 579–609.
(28) Valsamis, J.-B.; Mastrangeli, M.; Lambert, P. Vertical Excitation of Axisymmetric Liquid Bridges. *Eur. J. Mech. - BFluids* **2013**, *38*, 47–57.
(29) Kröger, R.; Berg, S.; Delgado, A.; Rath, H. J. Stretching Behaviour of Large Polymeric and Newtonian Liquid Bridges in Plateau Simulation. *J. Non-Newton. Fluid Mech.* **1992**, *45* (3), 385–400.
(30) Eggers, J.; Dupont, T. F. Drop Formation in a One-Dimensional Approximation of the Navier-Stokes Equation. *J. Fluid Mech.* **1994**, *262*, 205–221.
(31) Yildirim, O. E.; Basaran, O. A. Deformation and Breakup of Stretching Bridges of Newtonian and Shear-Thinning Liquids: Comparison of One- and Two-Dimensional Models. *Chem. Eng. Sci.* **2001**, *56* (1), 211–233.
(32) Donea, J.; Huerta, A.; Ponthot, J.-P.; Rodríguez-Ferran, A. Arbitrary Lagrangian–Eulerian Methods. In *Encyclopedia of Computational Mechanics*; John Wiley & Sons, Ltd, 2004.
(33) Hu, H. H.; Patankar, N. A.; Zhu, M. Y. Direct Numerical Simulations of Fluid–Solid Systems Using the Arbitrary Lagrangian–Eulerian Technique. *J. Comput. Phys.* **2001**, *169* (2), 427–462.
(34) Scardovelli, R.; Zaleski, S. Direct Numerical Simulation of Free-Surface and Interfacial Flow. *Annu. Rev. Fluid Mech.* **1999**, *31* (1), 567–603.
(35) Association, G. P. *Physical Properties of Glycerine and Its Solutions*; Glycerine Producers' Association, 1963.
(36) Coriell, S. R.; Hardy, S. C.; Cordes, M. R. Stability of Liquid Zones. *J. Colloid Interface Sci.* **1977**, *60* (1), 126–136.
(37) Snoeijer, J. H.; Andreotti, B. Moving Contact Lines: Scales, Regimes, and Dynamical Transitions. *Annu. Rev. Fluid Mech.* **2013**, *45* (1), 269–292.
(38) Dodds, S.; Carvalho, M.; Kumar, S. Stretching Liquid Bridges with Moving Contact Lines: The Role of Inertia. *Phys. Fluids 1994-Present* **2011**, *23* (9), 092101.
(39) Mastrangeli, M.; Arutinov, G.; Smits, E. C. P.; Lambert, P. Modeling Capillary Forces for Large Displacements. *Microfluid. Nanofluidics* **2014**, *18* (4), 695–708.

Table of content Graphic